Journal of Solid State Chemistry 183 (2010) 2616–2622

Contents lists available at ScienceDirect

Journal of Solid State Chemistry

journal homepage: www.elsevier.com/locate/jssc

Synthesis and phase width of new quaternary selenides $Pb_xSn_{6-x}Bi_2Se_9$ ($x=0$–4.36)

Kuei-Bo Chen, Chi-Shen Lee *

Department of Applied Chemistry, National Chiao Tung University, 1001 University Road, Hsinchu 30010, Taiwan

ARTICLE INFO

Article history:
Received 7 June 2010
Received in revised form
21 August 2010
Accepted 30 August 2010

Keywords:
Chalcogenide
Homologous
Lillianite
Thermoelectrics

ABSTRACT

Quaternary chalcogenides $Pb_xSn_{6-x}Bi_2Se_9$ ($x=0$–4.36) were synthesized with solid-state methods; their structures were determined from the X-ray diffraction of single crystals. $Pb_xSn_{6-x}Bi_2Se_9$ crystallizes in an orthorhombic space group *Cmcm* (No. 63); the structure features a three-dimensional framework containing slabs of NaCl-(3 1 1) type that exhibits identical layers containing seven octahedra units, which expand along the direction [0 1 0]. Each slab contains fused rectangular units that are connected to each other with *M*–Se contacts in a distorted octahedral environment. Calculations of the band structure, measurements of Seebeck coefficient and electrical conductivity confirm that these compounds are *n*-type semiconductors with small band gaps and large electrical conductivities.

1. Introduction

Chalcogenides with a heavy main-group element, such as Pb and Bi, are of great research interest, owing to their distorted coordination environments attributed to an inert electron pair, which might produce interesting structures and physical properties with possible thermoelectric applications [1–6]. Extensive research has been performed on multinary chalcogenide compounds, containing a heavy main-group element. These materials might exhibit enhanced thermoelectric properties of large electrical conductivities, small thermoconductivity, narrow band gap and long-term stability, which yield a large figure of merit (figure of merit ZT is defined as $ZT=TS^2\sigma/\kappa$ with S=Seebeck coefficient, σ=electrical conductivity and κ=thermal conductivity) [7–9]. Materials with *M*–Bi–*X* (*M*=Sn/Pb, *X*=S, Se, Te) contain various coordination environments constructed from M^{2+} (*M*=Sn, Pb) and M^{3+} (*M*=In, Sb, Bi) centers and an X^{2-} ion; the coordination environment for Pb^{2+}/Sn^{2+} ions is generally distorted and more complicated than that of Sb/Bi ions [10–12]. Chalcogenides with these main-group metal ions form interesting structure types, and some compounds exhibit suitable conductivities and excellent thermoelectric properties. [7,9,13,14]. Among these materials, minerals of the lillianite group exist as sulfides in ternary and quaternary systems; their structure is denoted as $L(n, n')$, in which n and n' are N values for two adjacent mirror-related layers. Particular attention has been devoted to the homologous series of the lillianite phase, because of their diverse structural types with an ordered intergrowth of 'NaCl-like' structures, cut parallel to the (3 1 1) plane [15–18].

Only few lillianite homologous series are reported for the quaternary selenides, containing heavy main-group elements Pb/Bi. We demonstrated that multinary selenides can be prepared through solid-state synthetic routes, after slow cooling of stoichiometric reaction products. Some related phases $InSn_2Bi_3Se_8$ [$L(1,3)$], $InSn_6BiSe_9$ [$L(7,7)$] [10], $Sn_2Pb_5Bi_4Se_{13}$ [$L(4,5)$] and $Sn_{8.65}Pb_{0.35}Bi_4Se_{15}$ [$L(4,7)$] [11] are reported. As the area is largely unexplored, one expects that various new compounds with interesting structures and properties can be discovered in the (Sn/Pb)–(Sb/Bi)–Se systems. While seeking new chalcogenides with group 4(Sn/Pb) and 5(Sb/Bi) metals, we prepared a new selenide solid solution, $Pb_xSn_{6-x}Bi_2Se_9$ ($x=0$–4.36); the structure is isostructural with mineral heyrovskyite [$L(7, 7)$] [15,19].

2. Experiments

2.1. Synthesis

All operations were performed in a glove box with a dry nitrogen atmosphere. Chemicals were used as obtained (from Alfa Aesar)—Bi, 99.5%, powder; Pb, 99.99%, powder; Sn, 99.9%; Sb, 99.9%, powder; Se, 99.95%, powder. The total masses of samples (all elements combined) were about 0.5 g. All reactants in evacuated fused-silica tubes were placed in resistance furnaces with a controlled temperature. The reaction mixture was heated from 300 to 1023 K over 8 h; the latter temperature was

* Corresponding author. Fax: +886 3 5723764.
E-mail address: chishen@mail.nctu.edu.tw (C.-S. Lee).

0022-4596/$ - see front matter © 2010 Elsevier Inc. All rights reserved.
doi:10.1016/j.jssc.2010.08.034

maintained for 16 h before natural cooling to about 300 K. The product contained a molten part and small particles with a metallic luster. The cuboid-shaped crystals were chosen for measurements of the X-ray diffraction on a single crystal.

2.2. Single-crystal X-ray diffraction (XRD)

Single crystals of compounds $Pb_xSn_{6-x}Bi_2Se_9$ ($x=0$ (**1**), 0.178 (**2**), 0.436 (**3**)) were mounted on glass fibers with epoxy glue; intensity data were collected on a diffractometer (Bruker APEX CCD) with graphite-monochromated Mo-$K\alpha$ radiation ($\lambda=0.71073$ Å) at 298(2) K. The distance from the crystal to the detector was 5.038 cm. Data were collected with a scan 0.3° in groups of 600, 435, 600 and 435 frames for each at settings 0°, 90°, 180° and 270°, respectively. The duration of exposure was 30 s for both samples; values of 2θ varied between 1.18° and 56.62°. Diffraction signals obtained from all frames of reciprocal space images were used to determine the parameters of the unit cell. The data were integrated (Siemens SAINT Program) and corrected for Lorentz and polarization effects [20]. Absorption corrections were based on a function fitted to the empirical transmission surface as sampled by multiple equivalent measurements of numerous reflections. The structural model was obtained with direct methods and refined with full-matrix least-square refinement based on F^2 (SHELXTL package) [21]. Crystallographic data and selected bond distances for $Sn_6Bi_2Se_9$, $Pb_{1.78}Sn_{4.22}Bi_2Se_9$ and $Pb_{4.36}Sn_{1.64}Bi_2Se_9$ are given in Tables 1–3. Further details of the crystal-structure investigation are obtainable from Fachinformationszentrum Karlsruhe, Eggenstein–Leopoldshafen, Germany (Fax: +49 7247 808 666; E-mail: crysdata@fiz.karlsruhe.de) on quoting the depository number CSD- 422136, 422135, and 422134.

2.3. Characterization

The X-ray powder-diffraction analysis of the products was performed, using Bragg–Brentano-type powder diffractometer (Bruker D8 Advance, operated at 40 kV and 40 mA, Cu $K\alpha$, $\lambda=1.5418$ Å). For phase identification, XRD data were collected over a 2θ range 5–90° with step interval 0.05°. The lattice parameters were calculated with least-squares fitting, using the CELREF program [22]. Energy-dispersive spectra (SEM/EDX, Hitachi S-4700I High-Resolution Scanning Electron Microscope) were recorded for the cuboid crystalline samples. The semiquantitative EDS analysis of individual crystals of each reaction product confirmed the presence of Sn, Pb, Bi and Se. Differential-thermal-analyzer (DTA) and thermogravimetric (TG) measurements were performed, using a thermal analyzer (NETZSCH STA 409PC). A powder sample (approximately 30 mg) was placed in an alumina crucible; Al_2O_3 powder served as a reference sample. The sample was heated to 1273 K at 20 K/min, under a constant flow of N_2.

2.4. Measurements of physical properties

Seebeck coefficients were measured on a cold-pressed bar ($1\times1\times5$ mm^3) with a commercial thermopower measurement apparatus (MMR Technologies) over the temperature range 300–500 K under a dynamic vacuum ($\sim10^{-2}$ Torr). Constantan served as an internal standard, and silver conductive paint was used to create electrical contacts. DC conductivity measurements were performed using a standard four-probe method with a homemade device under vacuum ($\sim10^{-2}$ Torr) over the temperature range 100–300 K. Electrical contacts consisted of four copper wires attached to the bulk with the silver cement. Samples were placed under vacuum at 295 K for at least 1 h to allow the silver glue to dry completely, which improved the contact performance. To minimize the effects of grain boundaries in the crystalline powder on the conductivity measurements, each cold-pressed sample was annealed at 773 K for 72 h before measurements.

2.5. Calculation of the electronic structure

Band calculations with tight-binding linear muffin-tin orbitals (LMTO) were undertaken to understand the electronic structures [23–27]. The space group *Cmcm* for $Pb_xSn_{6-x}Bi_2Se_9$ was used to simulate the observed crystal structures, containing mixed-occupancy sites (vide infra). Integration in the k space was performed with an improved tetrahedron method on grids of $16\times16\times8$ unique k points in the first Brillouin zone. We analyzed the electronic structure on extracting information from the band structure, densities of states (DOS), and crystal orbital-hamiltonian population curves (COHP) [28].

Table 1
Crystallographic data for $Pb_xSn_{6-x}Bi_2Se_9$ ($x=0$, 1.78 and 4.36).

Empirical formula	$Sn_6Bi_2Se_9$	$Pb_2Sn_4Bi_2Se_9$	$Pb_4Sn_2Bi_2Se_9$
Refined formula	$Sn_6Bi_2Se_9$	$Pb_{1.78}Sn_{4.22}Bi_2Se_9$	$Pb_{4.36}Sn_{1.64}Bi_2Se_9$
Formula weight (g/mol)	1840.74	1998.27	2226.6
Temperature (K)		300(2)	
Wavelength (Å)		0.71073	
Crystal system		Orthorhombic	
Space group		*Cmcm* (No. 63)	
Unit-cell dimensions (Å)	$a=4.206(2)$	$a=4.2105(8)$	$a=4.2469(7)$
	$b=13.903(6)$	$b=13.945(3)$	$b=14.073(2)$
	$c=32.12(1)$	$c=32.174(5)$	$c=32.383(5)$
Volume (Å^3)	1878(1)	1889.1(6)	1935.4(5)
Z		4	
Density (calculated) (g/cm^{-3})	6.510	7.026	7.641
Absorption coefficient (mm^{-1})	43.925	57.161	74.876
$F(0\,0\,0)$	3088	3316	3646
Crystal size (mm^3)	$0.03\times0.04\times0.2$	$0.03\times0.05\times0.3$	$0.03\times0.04\times0.2$
Reflections collected	4772	9994	11178
Independent reflections	1272 [R(int)=0.0901]	1357 [R(int)=0.0466]	1388 [R(int)=0.0431]
Data / restraints/parameters	1272/0/56	1357/0/60	1388/0/59
Goodness-of-fit on F^2	1.318	1.051	1.097
Final R indices [$I>2$sigma(I)]	$R1=0.0938$, $wR2=0.2685$	$R1=0.0353$, $wR2=0.0930$	$R1=0.0318$, $wR2=0.0773$
Largest diff. peak and hole (eÅ^{-3})	6.901 and −3.611	2.817 and −4.928	3.256 and −3.568

Table 2
Fractional atomic coordinates and equivalent isotropic atomic displacement parameters ($U_{eq}/10^{-3}$ Å^2) and site occupancies for $Sn_6Bi_2Se_9$.

	Site	x	y	z	sof	U(eq)[a]
M1	4a	0	0	0	Bi/Sn(0.40/0.60)	25(1)
M2	8f	0	0.2704(2)	0.4426(1)	100% Sn	24(1)
M3	8f	0	0.4553(2)	0.6180(1)	Bi/Sn(0.60/0.40)	22(1)
M4	8f	0	0.1769(2)	0.6732(1)	Bi/Sn(0.15/0.85)	20(1)
M5	4c	0	0.4109(6)	0.75	Bi/Sn(0.10/0.90)	97(1)
Se6	8f	0	0.3623(3)	0.5270(1)		23(1)
Se7	8f	0	0.0909(3)	0.5841(1)		22(1)
Se8	4c	0	0.2716(5)	0.75		25(1)
Se9	8f	0	0.1769(4)	0.3547(2)		31(1)
Se10	8f	0	0.0443(3)	0.6957(1)		24(1)
M1	4a	0	0	0	Pb/Bi/Sn(0.184/0.361/0.455(9))	22(1)
M2	8f	0	0.2706(1)	0.4423(1)	Pb/Bi/Sn(0.047/0.091/0.862(7))	18(1)
M3	8f	0	0.4551(1)	0.6182(1)	Pb/Bi/Sn(0.254/0.499/0.247(9))	21(1)
M4	8f	0	0.1783(1)	0.6732(1)	Pb/Bi/Sn(0.116/0.227/0.657(7))	22(1)
M5	4c	0	0.4134(1)	0.75	Pb/Sn(0.76(1)/0.24)	59(1)
Se6	8f	0	0.3626(1)	0.5269(1)		16(1)
Se7	8f	0	0.0899(1)	0.5842(1)		15(1)
Se8	4c	0	0.2697(1)	0.75		20(1)
Se9	8f	0	0.1756(1)	0.3544(1)		24(1)
Se10	8f	0	0.0452(1)	0.6953(1)		19(1)
M1	4a	0	0	0	Pb/Bi/Sn(0.529/0.315/0.156(8))	20(1)
M2	8f	0	0.2706(1)	0..4418(1)	Pb/Bi/Sn(0.389/0.231/0.380(7))	18(1)
M3	8f	0	0.4550(1)	0.6185(1)	Pb/Bi/Sn(0.577/0.343/0.081(7))	20(1)
M4	8f	0	0.1785(1)	0.6737(1)	Pb/Bi/Sn(0.448/0.267/0.285(7))	21(1)
M5	4c	0	0.4148(1)	0.75	100% Pb	58(1)
Se6	8f	0	0.3628(1)	0.5273(1)		16(1)
Se7	8f	0	0.0876(1)	0.5849(1)		15(1)
Se8	4c	0	0.2724(1)	0.75		23(1)
Se9	8f	0	0.1752(1)	0.3542(1)		24(1)
Se10	8f	0	0.0444(1)	0.6957(1)		20(1)

[a] (U_{eq}) is defined as one third of the trace of an orthogonalized U_{ij} tensor.

Table 3
Interatomic distances/Å for $Pb_xSn_{6-x}Bi_2Se_9$ ($x=0$, 1.78, and 4.36).

		$Sn_6Bi_2Se_9$	$Pb_{1.78}Sn_{4.22}Bi_2Se_9$	$Pb_{4.36}Sn_{1.64}Bi_2Se_9$
M1	—Se6 × 4	2.972(3)	2.9751(8)	3.0032(8)
	—Se7 × 2	2.979(4)	2.984(1)	3.015(1)
M2	—Se6 × 2	2.964(4)	2.9771(9)	3.0051(8)
	—Se6	2.996(5)	3.007(1)	3.058(1)
	—Se7 × 2	2.979(4)	2.9907(9)	3.0405(9)
	—Se9	3.108(2)	3.125(2)	3.139(2)
M3	—Se6	3.200(5)	3.211(1)	3.225(1)
	—Se7 × 2	3.028(4)	3.0275(9)	3.0288(9)
	—Se9 × 2	2.926(4)	2.9204(9)	2.9404(9)
	—Se10	2.783(5)	2.780(1)	2.799(1)
M4	—Se7	3.104(5)	3.118(1)	3.146(1)
	—Se8	2.798(4)	2.782(1)	2.802(1)
	—Se9 × 2	3.059(4)	3.061(1)	3.0922(9)
	—Se10 × 2	2.889(4)	2.896(1)	2.9292(9)
M5	—Se8 × 2	2.862(7)	2.906(1)	2.920(1)
	—Se9 × 2	3.578(2)	3.581(1)	3.604(1)
	—Se10 × 4	3.299(6)	3.302(1)	3.306(1)

3. Results and discussion

3.1. Synthesis and structure analysis

Ternary phase $Sn_6Bi_2Se_9$ (**1**) was obtained from an experiment with stoichiometric ratio '$Sn_6Bi_2Se_9$'; quaternary phases $Pb_{1.78}Sn_{4.22}Bi_2Se_9$ (**2**) and $Pb_{4.36}Sn_{1.64}Bi_2Se_9$ (**3**) were initially observed as a product from a reaction with molar ratios Pb:Sn:Bi:Se=3:8:4:17 and 3:1:2:7. The powder X-ray diffraction experiments from the products revealed an unknown phase after a search of the JCPDF database. The cuboid-shaped crystals were chosen for measurements on a single-crystal X-ray diffractometer. The refined formulae '$Sn_6Bi_2Se_9$,' '$Pb_{1.78}Sn_{4.22}Bi_2Se_9$' and '$Pb_{4.36}Sn_{1.64}Bi_2Se_9$' were determined, which was used to synthesize the pure phase with same heating conditions, as specified above. The experimental X-ray powder-diffraction patterns agreed satisfactorily with patterns simulated based on single-crystal data, confirming the phase purity of the products as synthesized (Fig. 1a). A series of reactions with $Pb_xSn_{6-x}Bi_2Se_9$ ($x=0$–6) were performed with the same heating conditions as specified above to investigate the phase width. Based on the powder X-ray diffraction, a pure phase of $Pb_xSn_{6-x}Bi_2Se_9$ was synthesized in the range $0 \le x \le 4$. Unknown and impurity phases of PbSe began to form when $x > 4$. Fig. 1b shows the refined lattice parameters for $Pb_xSn_{6-x}Bi_2Se_9$ ($x=0$–5). In general, the refined lattice parameters gradually increased as the proportion of Pb increased. The lattice parameters for samples with $x > 5.0$ could not be indexed, because of an impurity PbSe and an unknown phase overlapped on powder patterns with the major phase. Compared with single-crystal data of $Sn_6Bi_2Se_9$ (**1**), $Pb_{1.78}Sn_{4.22}Bi_2Se_9$ (**2**) and $Pb_{4.36}Sn_{1.64}Bi_2Se_9$ (**3**), the cell volume and average bond lengths of *M*–Se increase with increasing Pb concentration of the compound. This trend is consistent with the larger ionic radius of Pb^{2+} (1.29 Å) relative to Sn^{2+} (1.22 Å) [29]. Other possible variations in $Pb_xSn_{6-x}M_2X_9$ (M=Sb, Bi; X=S and Se) were tested; the products from the reaction contained mixtures of binary PbSe or SnSe or Bi_2Se_3 and an unknown phase.

$Sn_6Bi_2Se_9$ (**1**), *$Pb_{1.78}Sn_{4.22}Bi_2Se_9$* (**2**) *and* *$Pb_{4.36}Sn_{1.64}Bi_2Se_9$* (**3**) revealed an orthorhombic C-centered lattice; the analysis of systematic absences of reflections indicated space group *Cmcm* (No. 63). In the structure refinement, a structural model with five unique sites for metal atoms (Sn, Bi and Pb) and five unique sites for Se atoms was observed. Initially, the occupancy parameters

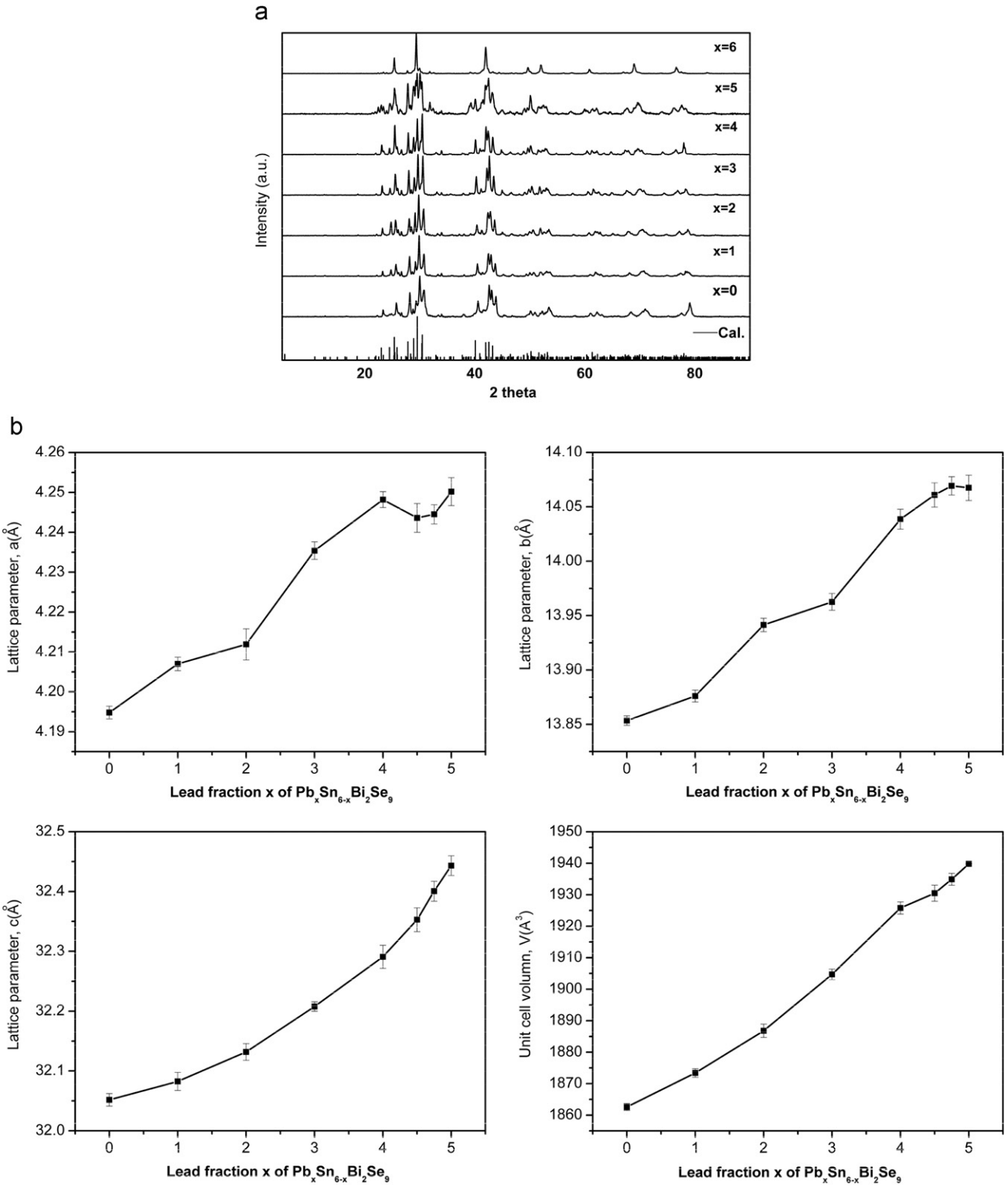

Fig. 1. (a) Experimental and simulated X-ray powder patterns for $Pb_xSn_{6-x}Bi_2Se_9$ ($x=0$–6). (b) The unit-cell volume and lattice parameters as a function of lead composition in $Pb_xSn_{6-x}Bi_2Se_9$ ($x=0$–5).

were refined with the fixed displacement parameters. The results show that all Se sites were fully occupied and *M*1–*M*5 sites have mixed occupancy. Quantitative analysis of Pb/Bi is difficult because of their similar atomic numbers. The Pb^{2+}/Bi^{3+} ratio in *M*1–*M*4 sites was thus fixed depending on a charge-balance model in quaternary systems. The refined electron densities produced direct evidence of the compositions of *M*1–*M*5 sites. The results presented as a function of Pb are shown in Fig. 2. The electron density of an *M*5 site is clearly increased significantly as the Pb element becomes included in the quaternary phase, indicative of a site preference for the Pb atom. In contrast, the electron densities of the *M*1–*M*4 sites are gradually increased upon substitution of the Pb atom. These results indicate that the Pb atom prefers to occupy the *M*5 site and shows no clear preference to occupy *M*1–*M*4 sites.

Based on the trend from the refined electron densities, the *M*1–*M*4 sites were refined with [(Pb/Bi)+Sn] with fixed ratio of Pb/Bi, whereas *M*5 sites were refined with [Sn+Pb]. Space groups of low symmetry were used to test whether the mixed occupied metal sites resulted from an incorrect choice of space group, with high symmetry. The results exhibit the same features of split metal sites, and the CCD frames of the intensity data revealed no evidence of superstructure reflections.

The final cycle of refinement included anisotropic displacement parameters and a secondary extinction correction performed on F_0^2. Fourier maps showed featureless residual maxima ~6.901, 3.256 and 2.82 e−/Å^3 near M5 for compounds **1**, **2** and **3**, respectively. The refined compositions are $(Sn^{+2})_6$ $(Bi^{+3})_2(Se^{-2})_9$ (**1**), $(Pb^{+2})_{1.78}$ $(Sn^{+2})_{4.22}$ $(Bi^{+3})_2(Se^{-2})_9$ (**2**) and $(Pb^{+2})_{4.36}$ $(Sn^{+2})_{1.64}$ $(Bi^{+3})_2(Se^{-2})_9$ (**3**), which agree with the reaction compositions.

3.2. Crystal structure

$Pb_xSn_{6-x}Bi_2Se_9$ is isostructural with the mineral heyrovskyite $Pb_6Bi_2S_9$ that crystallizes in an orthorhombic space group *Cmcm* (No. 63) with four formula units per unit cell. The structure contains ten crystallographically inequivalent sites, five for cations (Pb^{2+}, Sn^{2+}, and Bi^{3+}) and five for anions (Se^{2-}). Fig. 3 shows a [1 0 0] projection of the structure that comprises two slabs derived from NaCl (3 1 1) tilt planes expanded parallel to the *b*-axis, which are symmetry-related by mirror planes perpendicular to the *c*-axis (z=0, 1/2) and interconnected by Se atoms running along the *c*-axis. Each slab is composed of fused rectangular rod units that are expanded along the direction [1 0 0] and connected to each other with *M*–Se contacts in a distorted octahedral environment. The coordination environment of metal sites is grouped into three types: (i) site *M*1 is hexa-coordinate in a nearly ideal octahedron with an average *M*–Se distance 3.025 Å, which were refined as mixed occupancy with Pb/Bi/Sn. (ii) The coordination polyhedra around *M*2–*M*4 sites are distorted octahedral with a square pyramid having five short (2.78–3.06 Å) and one long (3.12–3.23 Å) bonds. This site has mixed occupancy Pb/Bi/Sn. (iii) The *M*5 site is located on the edge plane of two slabs that exhibit a bi-capped trigonal prism coordination environment. This site has mixed occupancy of Bi/Sn (**1**), Pb/Sn (**2**), and Pb (**3**). The *M*5–Se distances vary between 2.5 and 3.31 Å in a trigonal prism environment and two long *M*5–Se contacts between 3.58 and 3.6 Å, without bonding interaction. The *M*–Se distances in the $Pb_xSn_{6-x}Bi_2Se_9$ structures are comparable with other systems and some multinary selenides in the literature that contain mixed occupancy of Bi/Sn or Pb/Sn, such as $Pb_4Sb_4Se_{10}$ [30], $PbBi_2Se_4$ [31], $InSn_2Bi_3Se_8$ [10], and $Sn_2Pb_5Bi_4Se_{13}$ [11]. These compounds contain Sn, Bi, and Pb as the constituent elements with an electron lone pair that causes a distortion of the coordination environment.

The structures of $Pb_xSn_{6-x}Bi_2Se_9$ belong to the lillianite homologous series that is described with symbol $L(n, n')$, in which *L* indicates a member of the lillianite series and *n* and *n*′ correspond to the number of octahedra between two sides of the topochemical cell-twinning plane. The symbol $L(n, n')$ reflects the cation/anion ratio (*M*/*X*). The limit of the ratio *M*/*X* is located between 1 (PbS for $L(\infty,\infty)$) and 0.714 ($PbBi_4S_7$ for $L(2,1)$). The polysynthetic twinning in the NaCl-(3 1 1) type exhibits a ratio *M*/*X* decreasing with an increasing number of octahedral *n*. In the same way, symbol $L(7, 7)$ can be assigned for $Pb_xSn_{6-x}Bi_2Se_9$ (*M*/*X*=0.889). The structure can thus be considered to have a three-dimensional framework containing slabs of NaCl-(3 1 1) type that exhibits identical layers of seven octahedra wide slabs expanding along the direction [0 1 0].

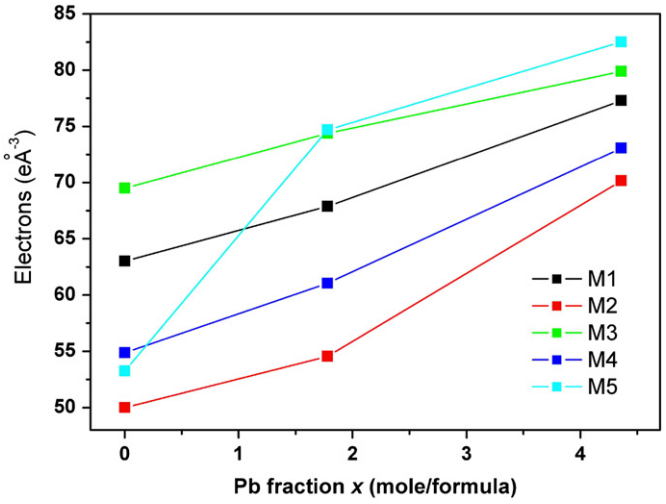

Fig. 2. Refined electronic densities of sites *M*1–*M*5 in the crystal data of $Pb_xSn_{6-x}Bi_2Se_9$ (x=0, 1.78, 4.36). The standard deviations are smaller than the symbols shown.

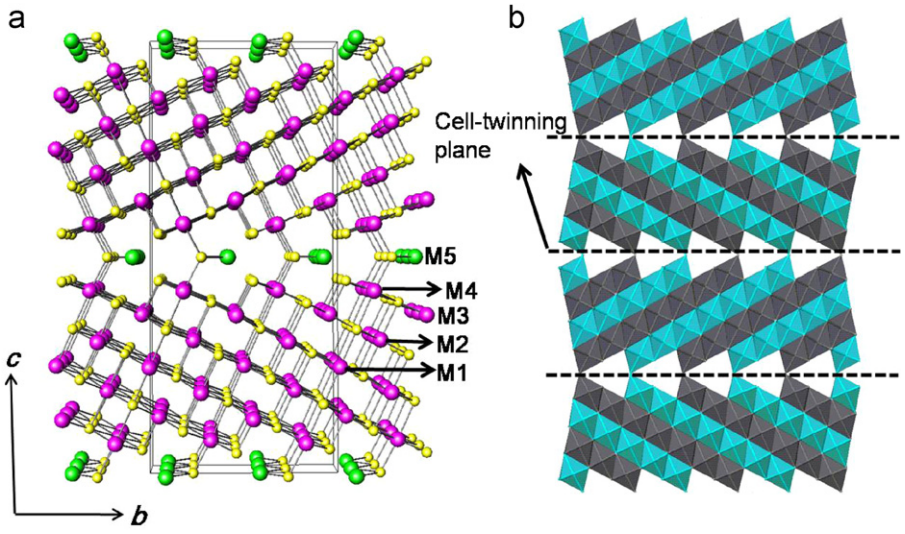

Fig. 3. Crystal structures of $Pb_xSn_{6-x}Bi_2Se_9$ (a) projection along the [1 0 0] direction with slight perspective and (b) representation, using blue and gray colors of octahedra.

3.3. Electronic structure

As the $Pb_xSn_{6-x}Bi_2Se_9$ phase exhibits a phase width with varied composition of Pb/Sn, we constructed three models with varied assignments of Pb, Bi and Sn in *M*1–*M*5 sites to perform calculations of the electronic structure (Table S1). These models generate hypothetical formulae $Sn_6Bi_2Se_9$ (**1**), $Pb_3Sn_3Bi_2Se_9$ (**2**) and $Pb_6Bi_2Se_9$ (**3**), respectively. Curves for the total and partial densities of states (DOS, PDOS) for these models appear in Fig. 4. The calculated band structures show direct band gaps for all models, indicative of filled valence bands with a semiconducting property. The electronic states near the Fermi level (E_F) are composed of mostly Pb(6p), Bi(6p) and Sn(5p) states. The large feature between −5 eV and the Fermi level is dominated by Se (3p) and Sn/Pb (5p/6p) states. The sharp features at −10 and −6 eV are from the filled *n*s state of Pb and Sn atoms.

The interatomic interactions for *M*–Se contacts were analyzed with the crystal orbital-hamiltonian population curves (COHP) and with an integration up to the Fermi level (–ICOHP). The assigned elements for metal sites *M*1, *M*2, *M*4, and *M*5 were gradually been replaced by the Pb atom, whereas the *M*3 site was fixed as Bi for all models. The results indicate that all *M*–Se contacts exhibit net bonding character with negative integrated crystal orbital-hamiltonian populations (Table 4). For model **1** ($Sn_3Bi_2Se_6$), the average –ICOHP for an Sn–Se contact is 4.25 eV/site; for model **3** ($Pb_3B_2S_6$), the average –ICOHP for the Pb–Se contact is 4.00 eV/site, indicative of strong bonding strength for an Sn–Se relative to Pb–Se contacts. The –ICOHP values were gradually decreased when these sites were exchanged from an Sn to Pb for *M*–Se (*M*=*M*1, *M*2, *M*4, and *M*5) contacts, and the deviations are within 8%. The deviation of –ICOHP for *M*5–Se is less than 1%, indicative of similar bonding strength for Pb–Se (4.21 eV/site) and Sn–Se contacts (4.17 eV/site). The results indicate that the Sn and Pb atoms might allow for a large exchange ratio in the site *M*5, which is consistent with the observed crystal data. The Bi–Se contact is assigned in an *M*3–Se for all models, which exists with a large –ICOHP 5.49 eV/site, indicative of strong interaction for the Bi–Se contact, consistent with the largest Bi occupancy for all crystal data.

3.4. Physical properties

A standard four-probe technique was used to measure the temperature-dependent conductivity from 100 to 300 K. The variation of specific electrical conductivities of $Pb_xSn_{6-x}Bi_2Se_9$ (x=0, 2 and 4 for i, ii and iii, respectively) with temperature is shown in Fig. 5a. The results exhibited a slightly increasing conductivity with an increasing temperature, consistent with the typical trend for a semiconducting property. For these compounds, the conductivity increased with an increasing Pb composition; whereas quaternary phase $Pb_4Sn_2Bi_2Se_9$ (iii) exhibited the largest conductivity near 295 K. Measurement of diffuse reflectance in the region 4000–400 cm^{-1} was not able to observe the optical band gaps for compounds **I**–**III**. This effect might be due to the mid-gap states derived from great mixed sites by aliovalent elements, such as Sn/Bi or Pb/Bi [32]. Compounds i–iii had a thermopower negative and are nearly independent of temperature, indicative of an *n*-type semiconducting behavior, in which most charge carriers are electrons (Fig. 5b). Near 295 K, the thermopower values were (i): −49.4, (ii): −42.4, and (iii): −26.1 μV/K, which are too small to be useful for TE applications.

3.5. Thermoanalyses

The curves of TG-DTA vs. temperature for solid solution compounds $Pb_xSn_{6-x}Bi_2Se_9$ (x=0, 2, and 4) showed similar results with an increased exothermic and decomposition maxima at ~1115 and ~1010 K, respectively (Figure S1). These results were reproduced on heating the powder, as synthesized in a silica ampoule, under vacuum and subsequently heating to 1173 K. The PXRD pattern of the residual product was indexed as a mixture of $SnSe_2$, PbSe, Bi_2Se_3, and Se phases.

4. Conclusions

Solid solutions $Pb_xSn_{6-x}Bi_2Se_9$ (x=0–4.36) were synthesized and characterized. The structure of $Pb_xSn_{6-x}Bi_2Se_9$ belongs to that of mineral heyrovskyite that contains slab units cut from the NaCl

Table 4
ICOHP values (eV/site) of the *M*–Se contacts from an integrated area of COHP curves.

Model	**I** $Sn_6Bi_2Se_9$	**II** $Sn_3Pb_3Bi_2Se_9$	**III** $Pb_6Bi_2Se_9$
*M*1	4.17	4.17	3.82
*M*2	3.98	3.98	3.70
*M*3	5.49	5.49	5.49
*M*4	4.65	4.32	4.32
*M*5	4.21	4.17	4.17

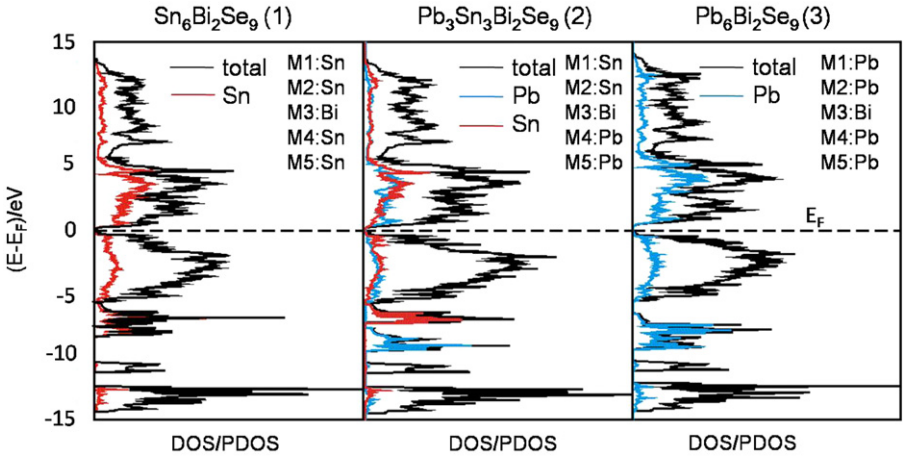

Fig. 4. DOS/PDOS curves for series of models: $Pb_xSn_{6-x}Bi_2Se_9$ (x=0, 3, 6). The black, red, and blue lines refer to total DOS, PDOS (Sn), PDOS (Pb), respectively. The horizontal dashed line denotes the Fermi energy (E_F). (For interpretation of the references to colour in this figure legend, the reader is referred to the web version of this article.)

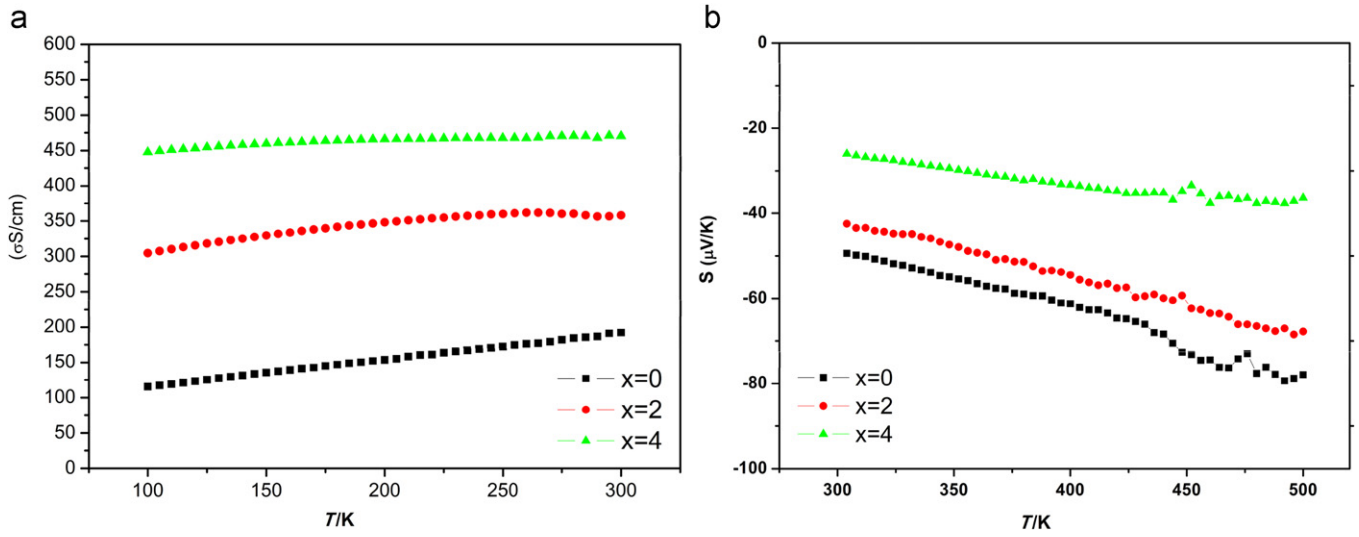

Fig. 5. Temperature dependence of electrical conductivity (a) and thermoelectric power (b) of $Pb_xSn_{6-x}Bi_2Se_9$ ($x=0$, 2, and 4).

structure parallel to the (3 1 1) plane. A significant correlation between the proportion of Pb and the lattice parameters was observed, which gradually increased as the composition of Pb increased. In these structures, Pb atoms can substitute for all cation sites with various Pb/Sn ratios especially in the *M*5 site, which is consistent with ICOHP results. As confirmed by measurements of physical properties and calculation of electronic structures, these phases are *n*-type semiconductors with small band gaps and large electrical conductivities.

Acknowledgment

National Science Council (NSC94-2113-M-009-012, 94-2120-M-009-014) supported this research.

Appendix A. Supporting information

Supplementary data associated with this article can be found in the online version at doi:10.1016/j.jssc.2010.08.034.

References

[1] K.S. Choi, D.Y. Chung, A. Mrotzek, P. Brazis, C.R. Kannewurf, C. Uher, W. Chen, T. Hogan, M.G. Kanatzidis, Chem. Mater. 13 (2001) 756–764.
[2] F.J. DiSalvo, Science 285 (1999) 703–706.
[3] L. Iordanidis, D. Bilic, S.D. Mahanti, M.G. Kanatzidis, J. Am. Chem. Soc. 125 (2003) 13741–13752.
[4] M.G. Kanatzidis, Semicond. Semimet. 69 (2001) 51–100.
[5] T.J. McCarthy, M.G. Kanatzidis, Inorg. Chem. 34 (1995) 1257–1267.
[6] J.O. Sofo, G.D. Mahan, Phys. Rev. B49 (1994) 4565–4570.
[7] K.F. Hsu, S. Loo, F. Guo, W. Chen, J.S. Dyck, C. Uher, T. Hogan, E.K. Polychroniadis, M.G. Kanatzidis, Science 303 (2004) 818–821.
[8] D.M. Rowe, CRC Handbook of Thermoelectrics, CRC Press, Boca Raton, FL, 1995.
[9] D.-Y. Chung, T. Hogan, P. Brazis, M. Rocci-Lane, C. Kannewurf, M. Bastea, C. Uher, M.G. Kanatzidis, Science 287 (2000) 1024–1027.
[10] M.F. Wang, S.M. Jang, J.C. Huang, C.S. Lee, J. Solid State Chem. 182 (2009) 1450–1456.
[11] K.B. Chen, C.S. Lee, Solid State Sci. 11 (2009) 1666–1672.
[12] M.F. Wang, W.H. Huang, C.S. Lee, Inorg. Chem. 48 (2009) 6402–6408.
[13] M.G. Kanatzidis, Acc. Chem. Res. 36 (2003) 111.
[14] M.G. Kanatzidis, Acc. Chem. Res. 38 (2005) 359–368.
[15] E. Makovicky, S. Karup-Moeller, Neues Jahrb. Mineral. Abh. 131 (1977) 56–82.
[16] B.G. Hyde, S. Andersson, M. Bakker, C.M. Plug, M. O'Keeffe, Prog. Solid State Chem. 12 (1980) 273–327.
[17] S. Misra, H.C. Padhi, J. Appl. Phys. 75 (1994) 4576.
[18] C.D. Lokhande, V.S. Yermune, S.H. Pawar, J. Electrochem. Soc. 138 (1991) 624.
[19] Y. Takeuchi, J. Takagi, J. Proc. Jpn. Acad. 50 (1974) 76–79.
[20] SAINT Version 6.22. Version, fourth ed., Siemens Analytical X-ray Instruments Inc., Madison, WI., 2001.
[21] SHELXTL Version 6.10. Reference Manual, Siemens Analytical X-ray Systems, Inc., Madison, WI., 2000.
[22] J. Laugier, B. Bochu, 〈http://www.inpg.fr/〉 LMGP; Laboratoire des Materiaux et du Génie Physique de l'Ecole Supérieure de Physique de Grenoble.
[23] O.K. Andersen, Phys. Rev. B 12 (1975) 3060–3083.
[24] H.L. Skriver, The LMTO Method, Springer, Berlin, 1984.
[25] U. van Barth, L. Hedin, J. Phys. C 4 (1971) 2064.
[26] P.E. Blöhl, O. Jepsen, O.K. Andersen, Phys. Rev. B 49 (1994) 16223–16233.
[27] O. Jepsen, O.K. Andersen, Z. Phys. 97 (1995) 25.
[28] R. Dronskowski, P.E. Blöhl, J. Phys. Chem. 97 (1993) 8617–8624.
[29] R.D. Shannon, Acta Crystallogr. Sect. A: Cryst. Phys. Diffr. Theor. Gen. Crystallogr. 32 (1976) 751–767.
[30] A. Skowron, I.D. Brown, Acta Crystallogr. Sect. C 46 (1990) 2287–2291.
[31] K.A. Agaev, S.A. Semiletov, Kristallografiya 13 (1968) 258–260.
[32] D.I. Bilc, S.D. Mahanti, M.G. Kanatzidis, Phys. Rev. B 74 (2006) 125202.